Supporting Information

Suppressing the Shuttle Effect and Dendrite Growth in Lithium-Sulfur Batteries

Jianan Wang,[†,§] Shanshan Yi,[†] Jianwei Liu,[†] Shiyi Sun,[†] Yunpeng Liu,[†] Duowen Yang,[†] Kai Xi,*[,‡,‖] Guoxin Gao,[†,§] Amr Abdelkader,[#] Wei Yan,*[,†,§] Shujiang Ding,*[,†,§] and Ramachandran Vasant Kumar[‖]

[†]Department of Environmental Science and Engineering, Department of Applied Chemistry, School of Chemistry, MOE Key Laboratory for Nonequilibrium Synthesis and Modulation of Condensed Matter, State Key Laboratory for Electrical Insulation and Power Equipment, Xi'an Jiaotong University, Xi'an 710049, China

[‡]Department of Engineering, University of Cambridge, Cambridge, CB3 0FA, United Kingdom

[‖]Department of Materials Science and Metallurgy, University of Cambridge, Cambridge, CB3 0FS, United Kingdom

[#]Faculty of Science and Technology, Bournemouth University, Talbot Campus, Fern Barrow, Poole, BH12 5BB, United Kingdom

[§]Xi'an Jiaotong University & Shaanxi Quantong Joint Research Institute of New Energy Vehicles Power, Xi'an 710049, China

*E-mail: dingsj@xjtu.edu.cn (S. Ding); yanwei@xjtu.edu.cn (W. Yan); kx210@cam.ac.uk (K. Xi)

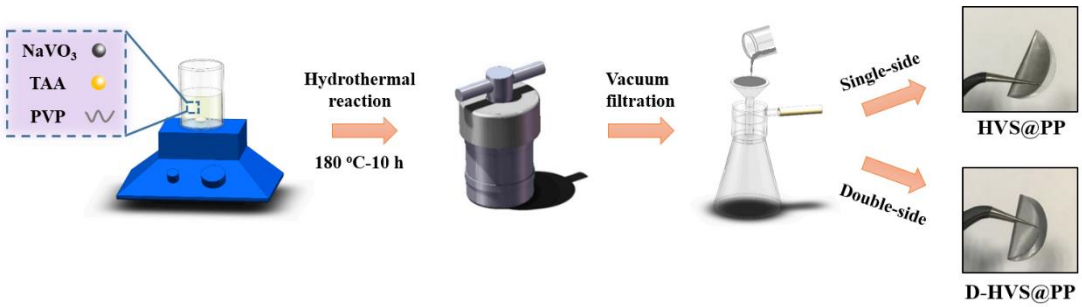

Figure S1. Schematic illustration of the fabrication process of the HVS modified separator.

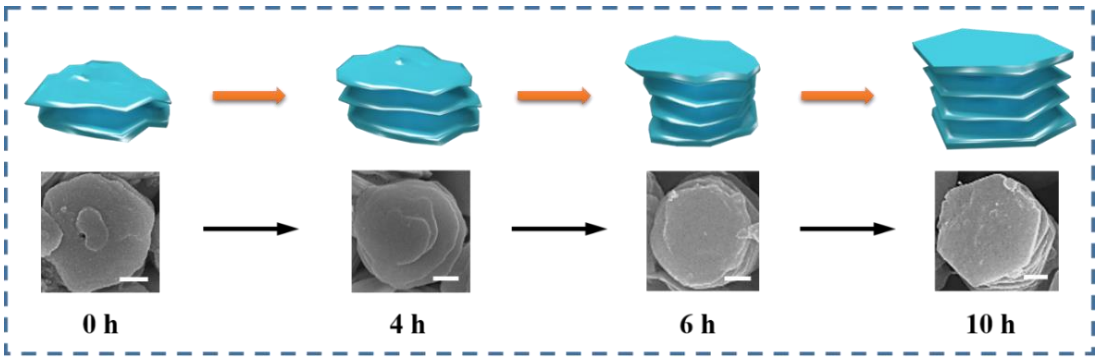

Figure S2. Schematic illustration and SEM images show the growth process of the VS_2 hexagonal nanosheets into the nanotower structure. The scale bar is 200 nm.

The possible formation mechanism of the VS_2 hexagonal nanotowers can be summarized as follow: In the first step, The VS_2 nanoflakes will be formed due to the inherent anisotropic growth of VS_2 planes, resulting from the large difference in the surface energy of various crystalline planes.[1] As the lowest surface energy of the (001) planes, the growth of hexagonal VS_2 nanoflakes along the ab-plane is favored.[2-4] The formed layered VS_2 structure is constituted by a metal vanadium layer between two sulfide layers to form a sandwich S-V-S, where the bonding between layers is controlled by weak van der Waals force.[5] In the same time, NH^{4+} from the $NH_3 \cdot H_2O$ will also be predominantly absorbed on the ab-plane of the VS_2 nanoflakes resulting in the positively charged VS_2 nanoflakes.[3] Hence, large PVP molecules as an anionic surfactant may be further absorbed on the surface of VS_2 layers due to electrostatic interactions.[6] With increasing the hydrothermal reaction time, the adsorbed PVP molecules can serve as a linking agent to bridge the adjacent VS_2 nanoflakes together, leading to the stacking of the nanoflake subunits along the c-axis to form the tower structure.[4, 6] Meanwhile, PVP also plays a vital role in controlling the size and

morphology of VS_2.[7] Driven by the crystal growth behavior of the hexagonal VS_2 and the interaction between PVP and the crystal surface, each nanosheet will gradually develop along the ab-plane from the irregular sheets to a perfect hexagonal structure through the Ostwald ripening method.[2] As a result, the final VS_2 hexagonal nanotowers can be formed.

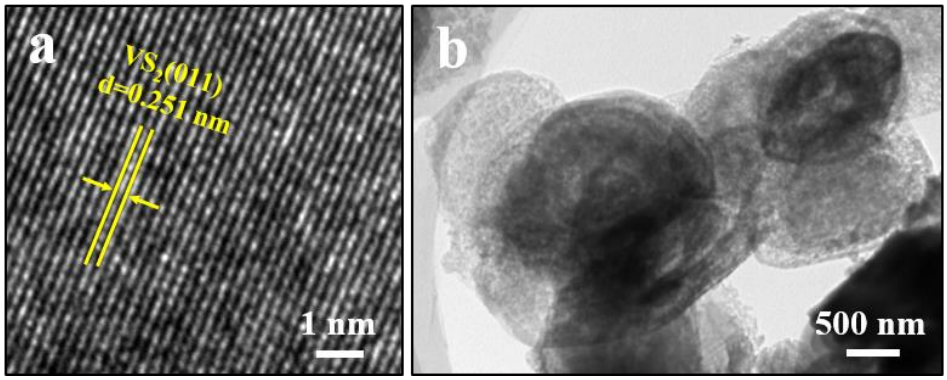

Figure S3. (a) HRTEM image of the HVS and (b) TEM image of the MVS.

HRTEM image of HVS in Figure S3a shows a clear d-spacing of 0.251 nm, corresponding to the (011) plane of a typical VS_2 crystal. The TEM image in Figure S3b further confirms the microflower morphology of the as-prepared MVS sample and the absence of any hexagonal nanosheets.

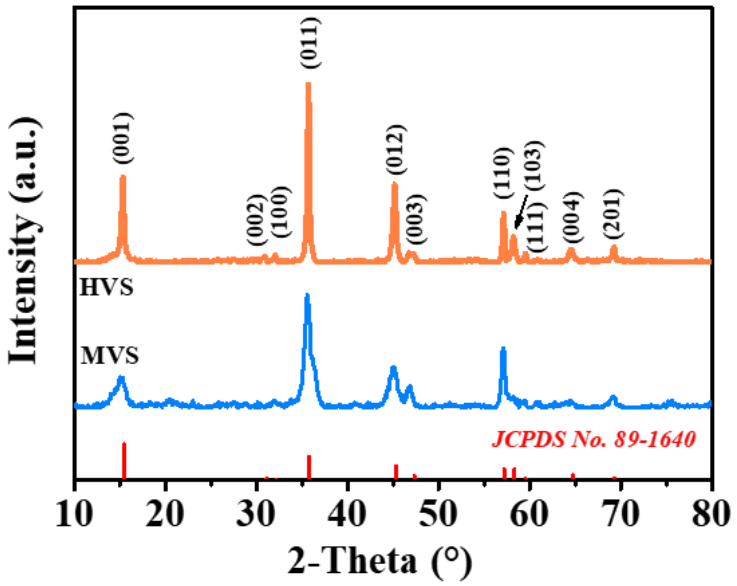

Figure S4. XRD spectra of the MVS and HVS samples.

For both the MVS and HVS samples, all the marked diffraction peaks match well to the hexagonal VS_2 (JCPDS No. 89-1640). The HVS exhibits sharper peaks compared with MVS, which implies that adding PVP K90 as a structure-directing agent into the VS_2 hydrothermal precursors is conducive to the crystallization of VS_2. No additional diffraction peaks are observed in the XRD curves of MVS and HVS, proving the high phase purity of the as-prepared VS_2 samples.

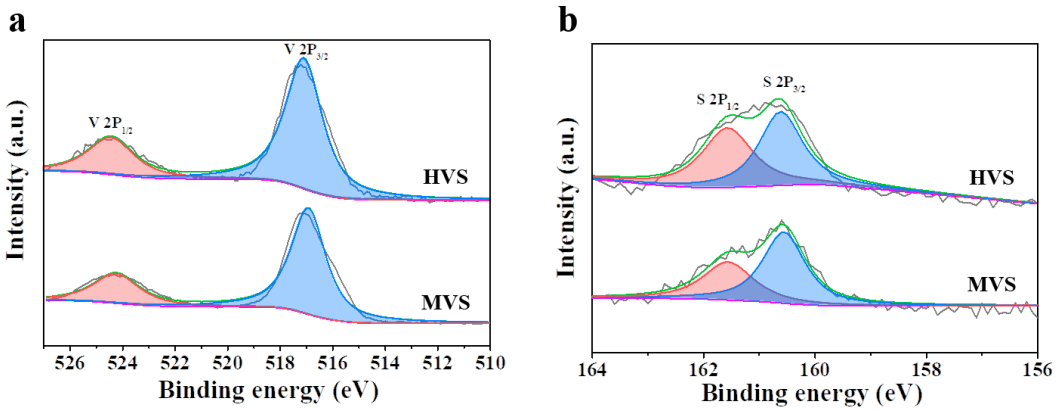

Figure S5. High-resolution XPS spectra of (a) V 2p and (b) S 2p of the MVS and HVS samples.

According to the high-resolution XPS results, MVS and HVS samples exhibit similar peak locations and relative intensity in both the V 2p and S 2p orbits. V 2p orbit can be divided by spin-orbit coupling into V $2p_{3/2}$ at 516.9 eV and V $2p_{1/2}$ at 524.3 eV, associated with the V^{4+} states. In addition, S $2p_{3/2}$ at 160.6 eV and S $2p_{1/2}$ at 161.6 eV are identified as S^{2-}. These results prove that VS_2 is the only chemical compound exist in both the MVS and HVS samples, consistent with the XRD analysis in (Figure S4).

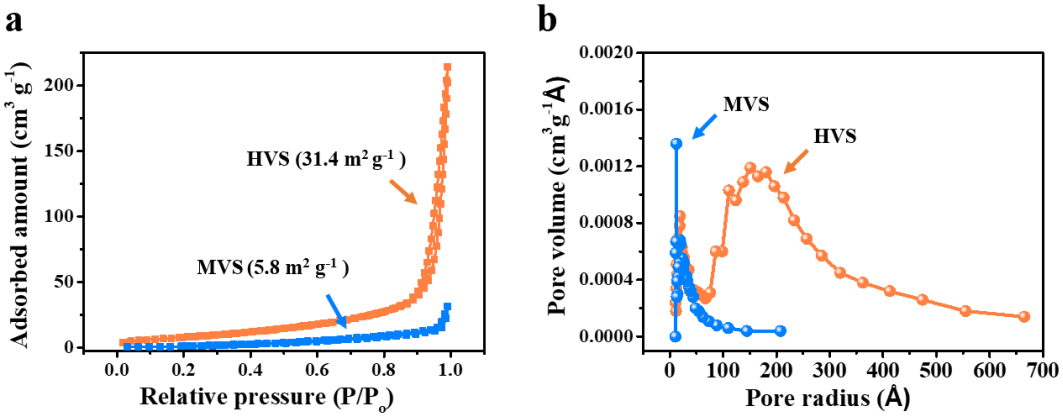

Figure S6. (a) N_2 adsorption–desorption analysis and (b) pore size distribution of the MVS and HVS samples.

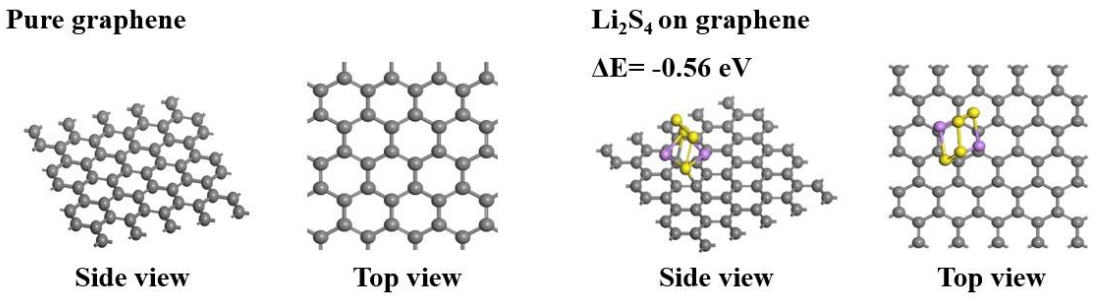

Figure S7. Density functional theory (DFT) calculation of the binding energy between the pure graphene and Li_2S_4 (VASP).

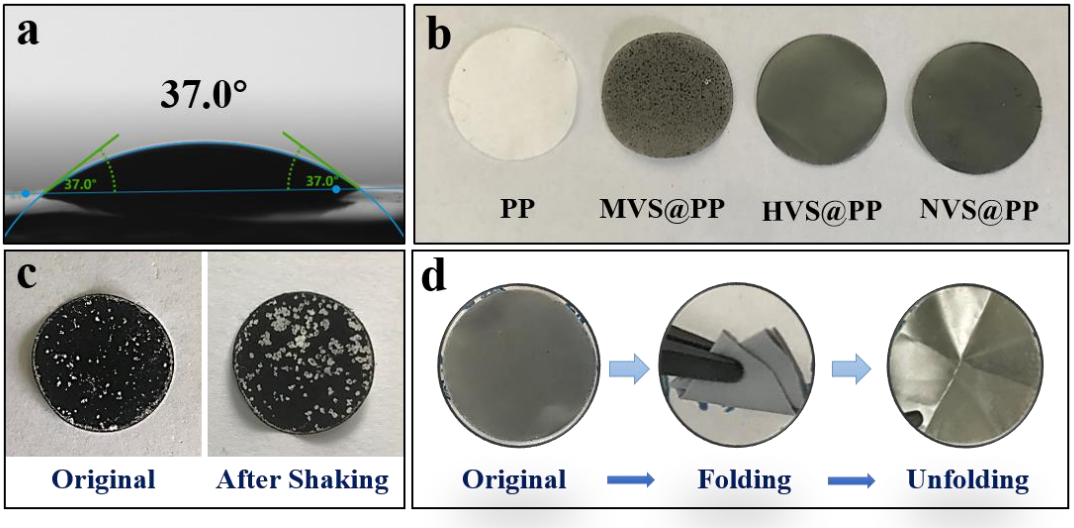

Figure S8. (a) Image of the contact angle of the pure PP separator; (b) Optical images of the PP, MVS@PP, HVS@PP and NVS@PP separators; (c) Super P@PP separator before and after shaking; (d) HVS@PP separator before and after folding.

The Super P@PP separator (Figure S8c) was obtained with the same vacuum filtration technique as the HVS@PP separator. Commercial Super P particles could be loosely coated onto the PP separator and were easily peeled off. For the HVS@PP separator, there existed a much strong adhesion between the HVS and PP separator. Therefore, no HVS fall-off was observed even after multiple folding (Figure S8d).

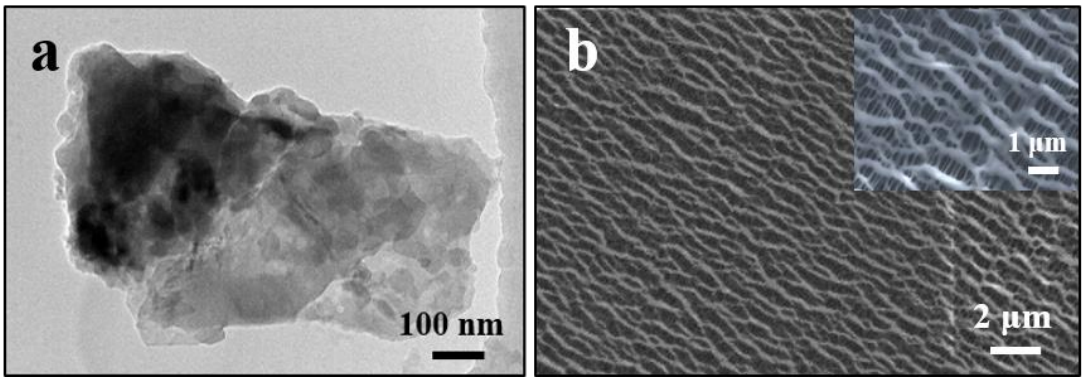

Figure S9. (a) TEM image of NVS; (b) SEM images of the pure PP separator.

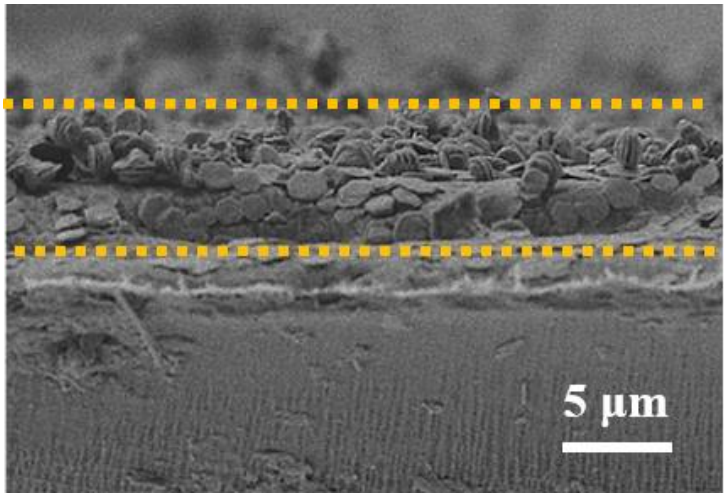

Figure S10. SEM image of the cross-section of the HVS@PP separator.

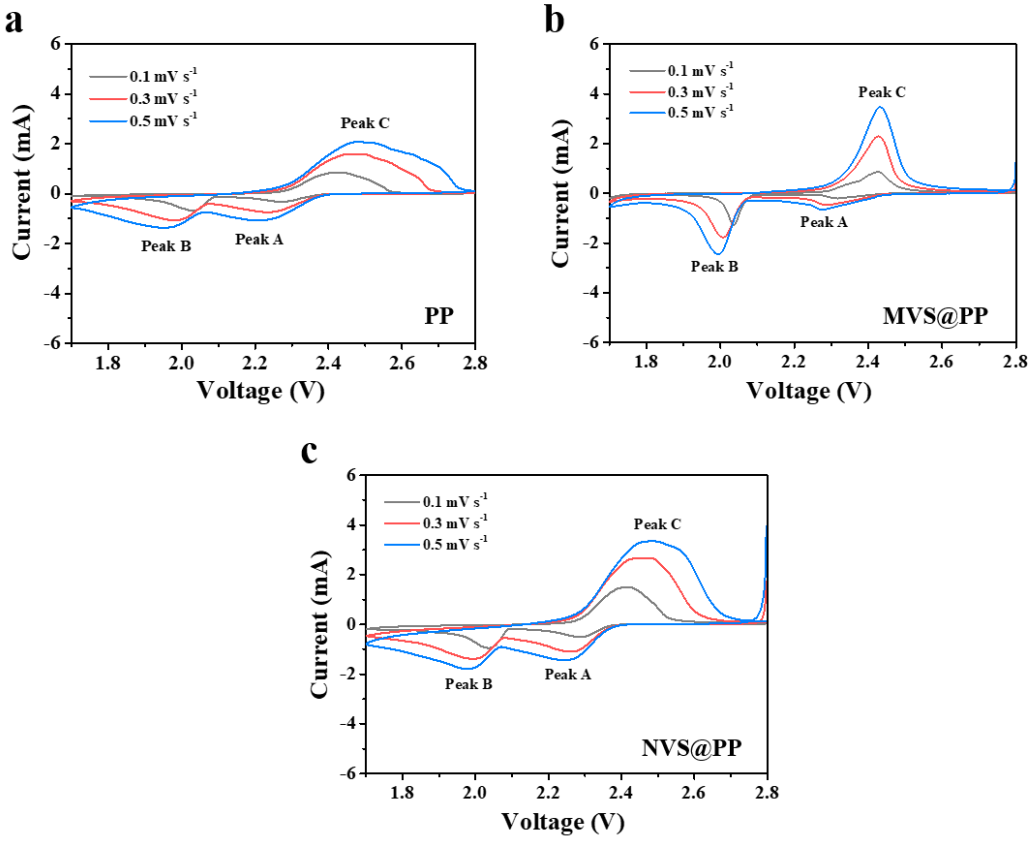

Figure S11. CV plots of (a) PP, (b) MVS@PP and (c) NVS@PP separators at various scan rates ranging from 0.1 to 0.5 $mV \cdot s^{-1}$ and a potential window of 1.7-2.8 V (vs. Li/Li^+). The first cathodic reduction process (peak A) represents the reduction reaction $S_8 \rightarrow Li_2S_x$. The second cathodic reduction process (peak B) is associated with the reaction $Li_2S_x \rightarrow Li_2S_2/Li_2S$. The anodic oxidation process (peak C) represents the oxidation of polysulfides to sulfur ($Li_2S_2/Li_2S \rightarrow S_8$).

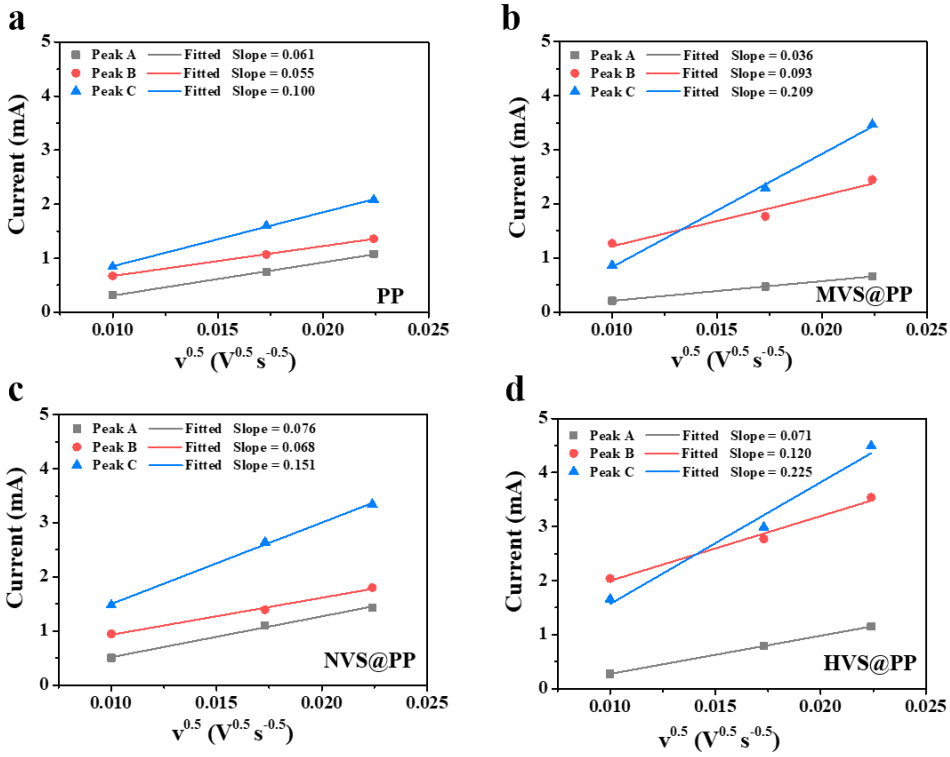

Figure S12. Plots of CV peak currents *vs.* the square root of the scan rates for the three peaks in Figure S11 for (a) PP, (b) MVS@PP, (c) NVS@PP and (d) HVS@PP separators.

According to the Randles-Sevcik equation,[8] the lithium diffusion process can be described by the following equation:

$$I_p = 2.69\times10^5 n^{1.5} A D_{Li^+}{}^{0.5} C_{Li^+} v^{0.5} \quad (1)$$

where I_p is the peak current, A; n is the electron transfer number, n=2 for Li–S cells; A is the electrode area, cm^2; D_{Li^+} is the lithium-ion diffusion rate, $cm^2\ s^{-1}$; C_{Li^+} is the Li^+ concentration in the electrolyte, mol mL^{-1}; v is the scan rate, V s^{-1}. The slope of the fitted line ($I_p/v^{0.5}$) represents the lithium-ion diffusion rate when I_p has a linear correlation with $v^{0.5}$.

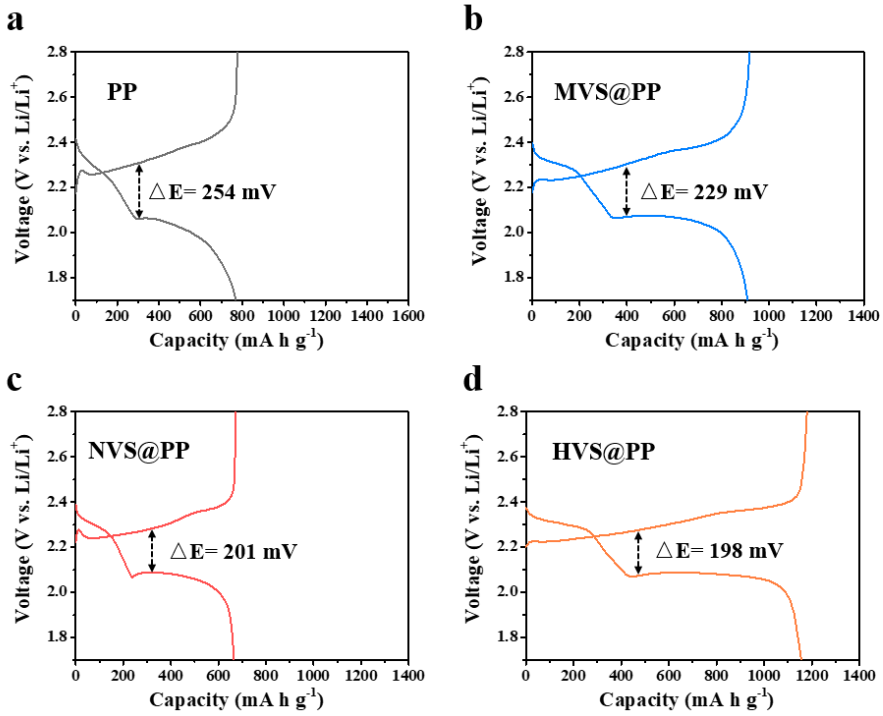

Figure S13. Galvanostatic charge/discharge proles for the first cycles at 0.2 C: (a) PP, (b) MVS@PP, (c) NVS@PP and (d) HVS@PP separators.

Figure S13 shows the first galvanostatic charge/discharge cycle of the four separators at 0.2 C. The polarization (△E) of the four separators can be determined from the figures to be 229, 201, 198 mV, and 254 mV for the MVS@PP, NVS@PP, HVS@PP, and pure PP separators, respectively. The VS_2 particles on the PP have resulted in lower polarization as compared with the conventional PP separator, proving that introducing the conductive VS_2 layer onto the PP separator is beneficial to reduce the interfacial resistance between cathode and separator, hence achieving a more efficient sulfur redox kinetics.[9, 10]

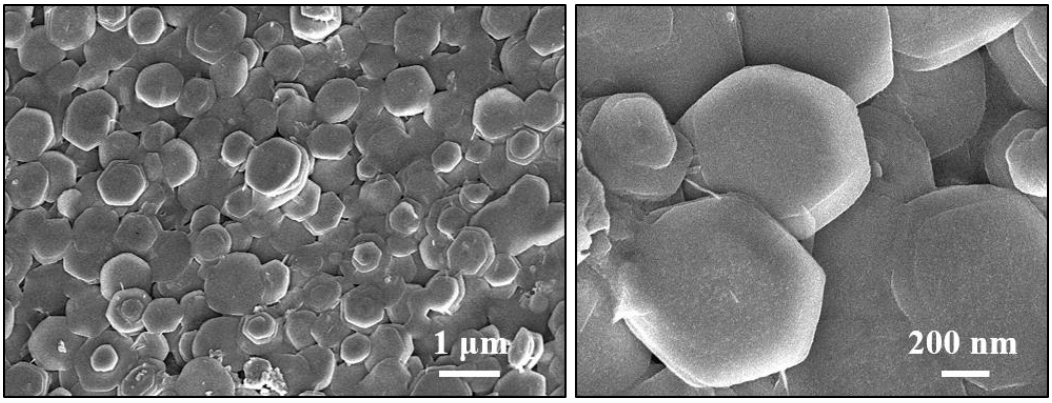

Figure S14. SEM images of the HVS@PP separator (sulfur cathode side) after 300 cycles.

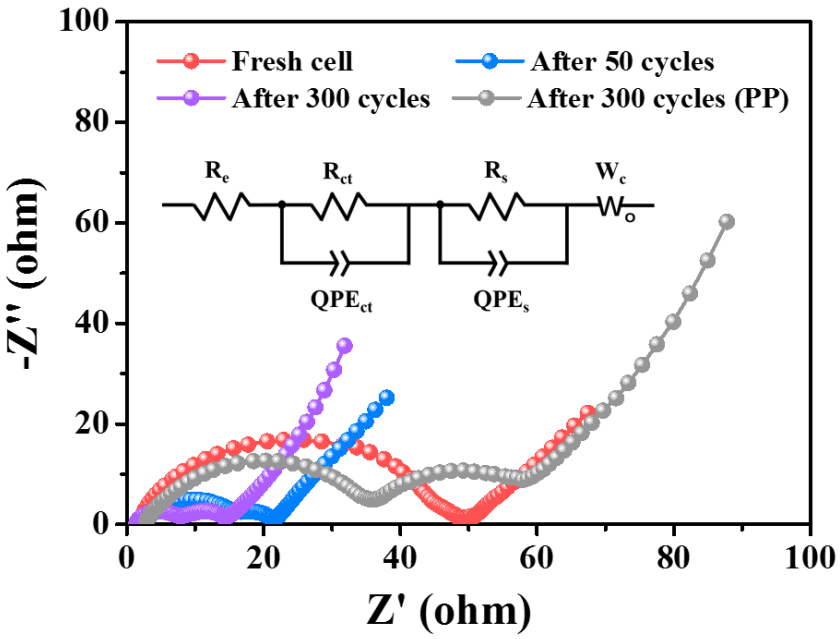

Figure S15. EIS plot of the HVS@PP separator tested at open-circuit voltage, after 50 and 300 cycles and the PP separator after 300 cycles.

The resistance of the HVS@PP separator decreased gradually with cycling, which might lead to an improvement in the sulfur redox kinetics.

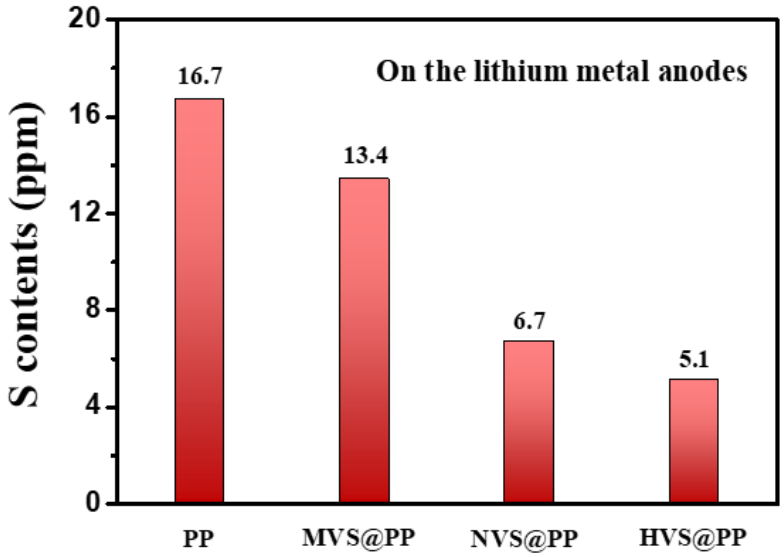

Figure S16. The sulfur deposited on the lithium metal anodes for various separators after 300 cycles. The sulfur content was measured by ICP-AES.

The lithium metal anode was dissolved in water and then used for ICP-AES analysis. The HVS@PP clearly showed the best performance in suppressing the Li_2S_x formation.

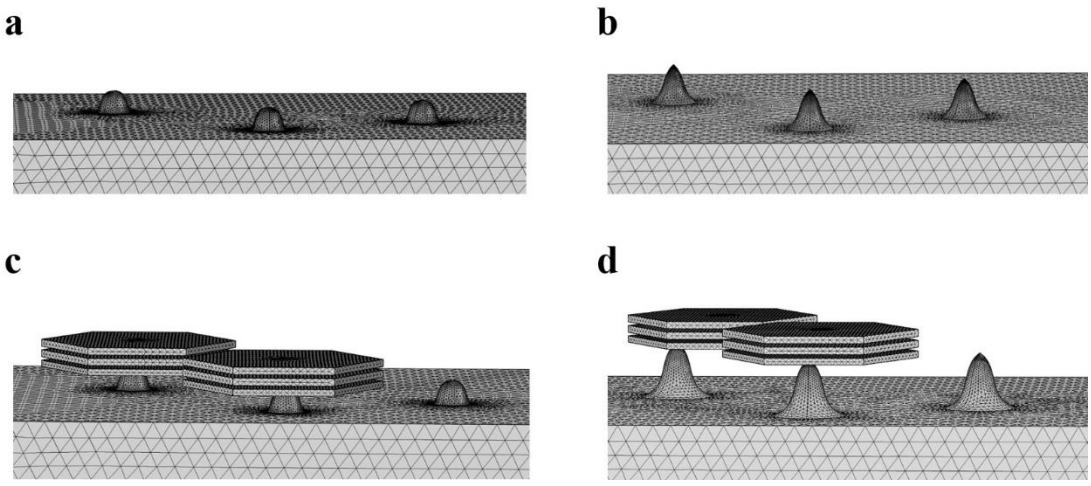

Figure S17. The corresponding constructed models in Figure 4d-g with the extremely refined physical field-controlled grids for accurate COMSOL Multiphysics simulation.

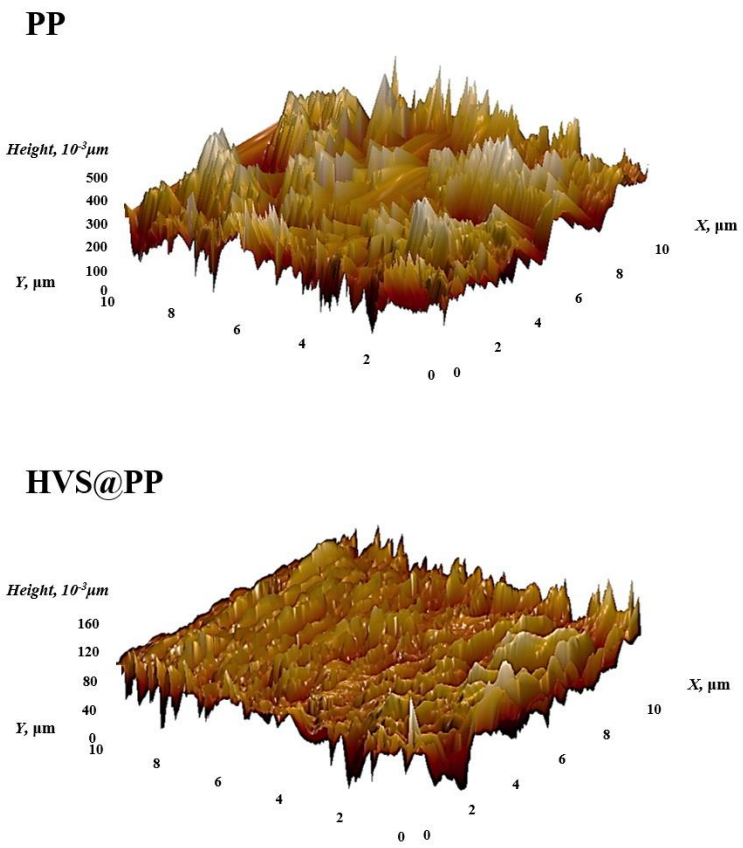

Figure S18. AFM images of the surfaces of the lithium metal anode in the Li || Li symmetric cells with PP and D-HVS@PP separators after 100 cycles.

The lithium anode was able to maintain a smoother surface when the D-HVS@PP separator was used as compared with the commercial PP separator. The smoother surface is clear evidence of the great ability of the D-HVS@PP separator to suppress the lithium dendrites growth.

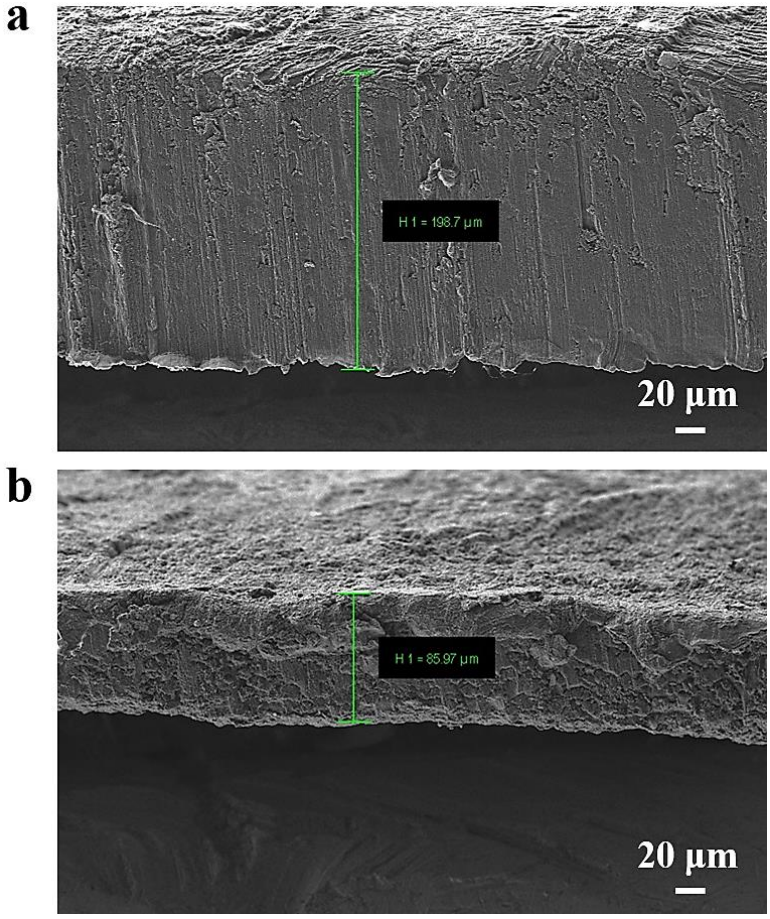

Figure S19. SEM images of the cross-section of (a) 200 µm and (b) 85 µm thick lithium-metal foils.

The practical thickness for the defined 200 and 85 µm lithium-metal foils were 198.7 and 85.97 µm, respectively, measured by the own imaging analysis software of GeminiSEM500.

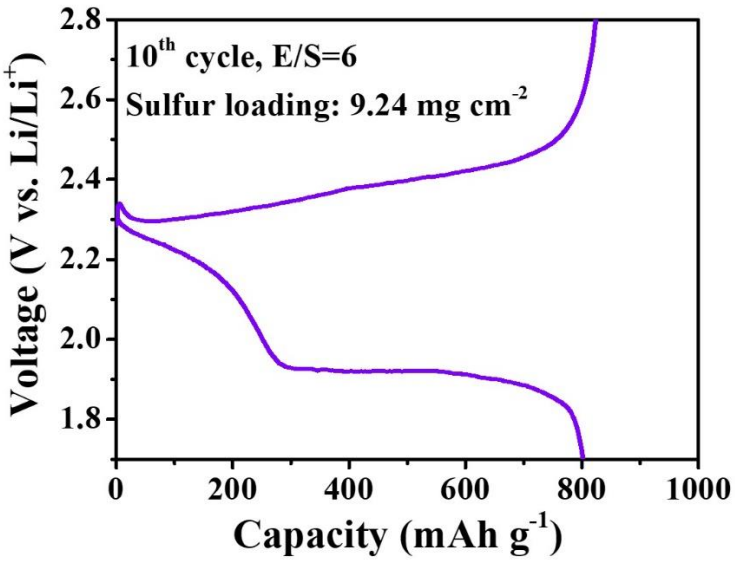

Figure S20. Galvanostatic charge/discharge profile of D-HVS@PP separator at 10th cycle at 0.2 C.

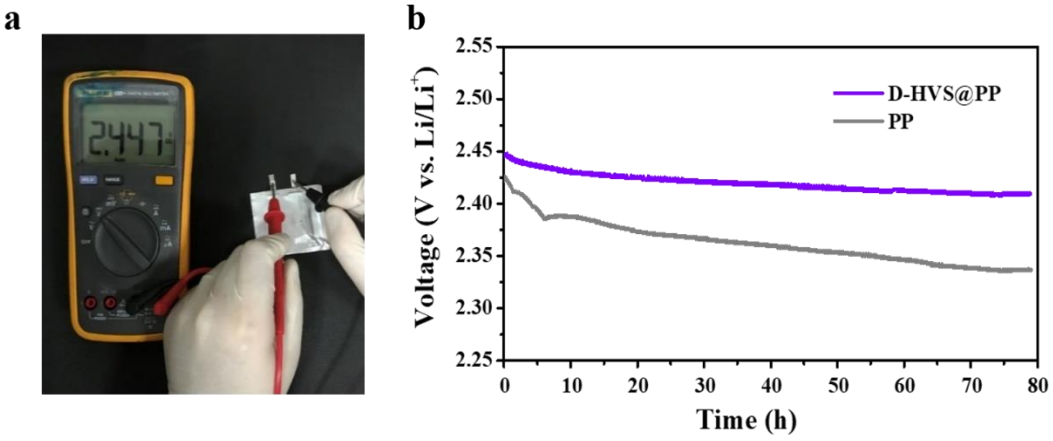

Figure S21. (a) The open-circuit voltage of the pouch Li-S batteries with D-HVS@PP separator; (b) The self-discharge monitoring for the pouch Li-S batteries with the PP and D-HVS@PP separators.

The self-discharge phenomenon was investigated by continuously monitoring the open-circuit voltages of the pouch Li-S batteries with the PP and D-HVS@PP separators. Compared with the conventional PP separator, the D-HVS@PP separator exhibited a higher and more stable open-circuit voltage even after 80 h, suggesting its better ability to depress the self-discharge phenomenon in Li-S battery.[11, 12]

Table S1. Comparisons of the lithium-ion diffusion rate (D_{Li^+}) of various separators.

Materials	Lithium-ion diffusion rate D_{Li^+} ($cm^2\ s^{-1}$)		
	Peak A	Peak B	Peak C
PP	6.4×10^{-9}	5.2×10^{-9}	1.7×10^{-8}
MVS@PP	2.2×10^{-9}	1.5×10^{-8}	7.6×10^{-8}
NVS@PP	1.0×10^{-8}	8.0×10^{-9}	3.9×10^{-8}
HVS@PP	8.7×10^{-9}	2.5×10^{-8}	8.8×10^{-8}

The lithium-ion diffusion rate (D_{Li^+}) was calculated based on the Randles-Sevcik equation as described in Figure 3c and Figure S12. In this work, the constant parameters are: n=2, A=1.54 cm^2, $C_{Li^+}=10^{-3}$ mol mL^{-1}.

Table S2. Impedance data calculated from EIS results shown in Figure 3d and Figure S15.

Batteries	R_e (Ω)	R_{ct} (Ω)	R_s (Ω)
Fresh cell (PP)	3.0	71.7	-
Fresh cell (MVS@PP)	1.7	56.3	-
Fresh cell (NVS@PP)	2.0	87.2	-
Fresh cell (HVS@PP)	1.7	45.8	-
After 50 cycles (HVS@PP)	2.6	13.5	3.5
After 300 cycles (HVS@PP)	1.4	6.3	5.2
After 300 cycles (PP)	2.6	33.8	12.7

The impedance data were calculated based on the equivalent electrical circuit models for the EIS plots in Figure 3d and Figure S15. Where R_e is electrolyte resistance, R_{ct} and QPE_{ct} denote the charge-transfer resistance and relative double-layer capacitance; R_s and QPE_s represent the resistance and capacitance of the SEI film formed at the separator/electrode interface; W_c represents the Warburg impedance.[13, 14]

Table S3. Calculations of the N/P ratio in the current Li-S coin and pouch batteries assembled by D-HVS@PP separators.

Batteries-Li thickness (μm)	**Cathode (PE)**				**Anode (NE)**				**N/P ratio**
	Electrode area (cm^2)	Active material loading (mg cm^{-2})	Areal specific capacity (mAh cm^{-2})	Specific capacity (mAh)	Electrode area (cm^2)	Active material loading (mg cm^{-2})	Areal specific capacity (mAh cm^{-2})	Specific capacity (mAh)	
Li-S coin battery-200	1.54	9.24	15.48	23.84	2.01	10.68	41.22	82.85	3.5
Li-S coin battery-85	1.54	8.13	13.62	20.97	2.01	4.54	17.52	35.22	1.7
Li-S pouch battery-200	8.75	7.25	12.14	106.23	8.75	10.68	41.22	360.68	3.4

*The defined specific capacity is 1675 mAh g^{-1} for sulfur and 3860 mAh g^{-1} for lithium. The diameters of the cathode and the anode discs in the coin batteries were fixed to be 14 and 16 mm, respectively. The sizes of both the cathode and anode in pouch batteries were 2.5 cm×3.5 cm.

Table S4. Comparisons of the areal capacities between the D-HVS@PP separator at a high sulfur loading and other similar materials reported.

Materials	Sulfur loading (mg cm^{-2})	Initial Areal capacity (mAh cm^{-2})	Initial capacities (mAh g^{-1})	Capacities after cycling (mAh g^{-1})	Cycle number	Current density	Reference
VS_2 nanoflowers/S cathode	1.68	1.72	1026.6	~700	200	0.2 C	15
S-VS_2@G/CNT cathode	0.73	0.61/ 0.80 (0.2 C)	830/ 1,093 (0.2 C)	701	300	0.5 C	8
rGO-VS_2/S cathode	1.8	2.2	1194	929	200	0.2 C	16
FeS_2/FeS/S cathode	1.0	1.2	~1200	1045	30	0.1 C	17
MoS_2/Celgard separator	-	-	808	401	600	0.5 C	12
MoS_2-Polymer modified separator	4.0	~3.2/ ~4.2 (0.2 C)	~800/ ~1050 (0.2 C)	~500	400	1.0 C	18
Co_9S_8-Celgard separator	5.6	5.5	985	830	200	0.1 C	19
a-Ti_3C_2-S/d-Ti_3C_2/PP separator	1.0	0.9	899	611	50	0.5 C	20
Black phosphorus modified separator	2	1.9	930	800	100	0.24 C	21
V_2O_5 NWs/graphene nanoscrolls interlayer	3.3	2.6	790	435	400	0.2 C	22
HVS@PP separator	1.5	1.7	1156	908	300	0.2 C	This work
D-HVS@PP separator-85	8.13	8.4	1028	501	150	0.2 C	This work
D-HVS@PP separator-200	9.2	8.3	905	647	120	0.2 C	This work

Table S5. Calculations of the areal weight for various Li-S batteries.

Batteries (Li thickness)	**Current collector** (mg cm^{-2})	**Active layer** (mg cm^{-2})	**Separator** (mg cm^{-2})	**Electrolyte** (mg cm^{-2})	**Li anode** (mg cm^{-2})	**Total weight** (mg cm^{-2})
Conventional Li-S battery	5.33 (Al foil)	2.14 (active S = 1.5 mg cm^{-2})	1.24 (PP)	25.80 (23 μL, E/S=15)	21.36 (thickness ~ 400 μm)	55.87
Li-S coin battery-200 (In this work)	1.30 (CNFs)	13.20 (active S = 9.24 mg cm^{-2})	1.38 (D-HVS@PP)	61.60 (55 μL, E/S=6)	10.68 (thickness ~ 200 μm)	88.16
Li-S coin battery-85 (In this work)	1.55 (CNFs)	11.61 (active S = 8.13 mg cm^{-2})	1.38 (D-HVS@PP)	35.84 (32 μL, E/S=4)	4.54 (thickness ~ 85 μm)	54.92

*The mass of electrolyte is measured to be 1.12 mg ul^{-1}; The density of Li anode is 0.534 g cm^{-3}; The mass ratio of the active sulfur to the whole active layer was 70%.

In Figure 6c and Table S5, the area weights of various components in conventional Li-S battery were provided based on the previous literature data.[10, 23, 24] The conventional Li-S batteries were commonly assembled by an Al foil current collector with low sulfur areal loading (<2.0 mg cm^{-2}), a widely used and thick commercial lithium (>400 μm) and a high E/S ratio (>15 mL g^{-1}). In this work, to evaluate the performance of D-HVS@PP separator in practical Li-S batteries, the Li-S cells were assembled by a lighter CNFs current collector with high sulfur areal loading, and a thinner lithium anode and a lower E/S ratio. In addition, lithium foils with different thickness (200 μm

and even 85 μm) were tested as the anode to further control the N/P ratio of batteries, as shown in Table S3.

The cell-level gravimetric energy density values for Li-S coin battery-200 and Li-S coin battery-85 were also calculated based on the whole basic units of battery system (neglecting the mass of any packaging material), as shown in the following formula[23]:

$$\frac{\text{Capacity mAh g}^{-1} \times 2.15\ \text{V} \times \text{mass(S) mg cm}^{-2}}{(m_{Current\ collector} + m_{Active\ layer} + m_{Electrolyte} + m_{Separator} + m_{Li})\ \text{mg cm}^{-2}} \quad (2)$$

The cell-level gravimetric energy density value (1st cycle) for Li-S coin battery-200:

$905 \times 2.15 \times 9.24/88.16 = 204\ \text{Wh kg}_{cell}^{-1}$

The cell-level gravimetric energy density value (1st cycle) for Li-S coin battery-85:

$1028 \times 2.15 \times 8.13/54.92 = 327\ \text{Wh kg}_{cell}^{-1}$

Notably, for the high loading of the Li-S batteries, the low E/S ratio and thin lithium anode is critical for reducing the total battery weight and consequently achieving a high cell-level gravimetric energy density.

REFERENCES

1. Muller, G. A.; Cook, J. B.; Kim, H. S.; Tolbert, S. H.; Dunn, B. High Performance Pseudocapacitor Based on 2D Layered Metal Chalcogenide Nanocrystals. *Nano Lett.* **2015**, *15*, 1911-1917.

2. Fang, Z.; Hao, S.; Long, L.; Fang, H.; Qiang, T.; Song, Y. The Enhanced Photoelectrochemical Response of $SnSe_2$ Nanosheets. *CrystEngComm* **2014**, *16*, 2404.

3. Feng, J.; Sun, X.; Wu, C.; Peng, L.; Lin, C.; Hu, S.; Yang, J.; Xie, Y. Metallic Few-Layered VS_2 Ultrathin Nanosheets: High Two-Dimensional Conductivity for In-Plane Supercapacitors. *J. Am. Chem. Soc.* **2011**, *133*, 17832-17838.

4. Chen, J. S.; Liu, J.; Qiao, S. Z.; Xu, R.; Lou, X. W. Formation of Large 2D Nanosheets *via* PVP-Assisted Assembly of Anatase TiO_2 Nanomosaics. *Chem. Commun.* **2011**, *47*, 10443-10445.

5. Sun, R.; Pei, C.; Sheng, J.; Wang, D.; Wu, L.; Liu, S.; An, Q.; Mai, L. High-Rate and Long-Life VS_2 Cathodes for Hybrid Magnesium-Based Battery. *Energy Storage Mater.* **2018**, *12*, 61-68.

6. Sun, R.; Wei, Q.; Sheng, J.; Shi, C.; An, Q.; Liu, S.; Mai, L. Novel Layer-By-Layer Stacked VS_2 Nanosheets with Intercalation Pseudocapacitance for High-Rate Sodium Ion Charge Storage. *Nano Energy* **2017**, *35*, 396-404.

7. Koczkur, K. M.; Mourdikoudis, S.; Polavarapu, L.; Skrabalak, S. E. Polyvinylpyrrolidone (PVP) in Nanoparticle Synthesis. *Dalton Trans.* **2015**, *44*, 17883-17905.

8. Zhou, G.; Tian, H.; Jin, Y.; Tao, X.; Liu, B.; Zhang, R.; Seh, Z. W.; Zhuo, D.; Liu, Y.; Sun, J.; Zhao, J.; Zu, C.; Wu, D. S.; Zhang, Q.; Cui, Y. Catalytic Oxidation of Li_2S

on the Surface of Metal Sulfides for Li-S Batteries. *P. Natl. Acad. Sci.* **2017**, *114*, 840-845.

9. Zhu, P.; Zhu, J.; Zang, J.; Chen, C.; Lu, Y.; Jiang, M.; Yan, C.; Dirican, M.; Kalai Selvan, R.; Zhang, X. A Novel Bi-Functional Double-Layer RGO-PVDF/PVDF Composite Nanofiber Membrane Separator with Enhanced Thermal Stability and Effective Polysulfide Inhibition for High-Performance Lithium-Sulfur Batteries. *J. Mater. Chem. A* **2017**, *5*, 15096-15104.

10. Li, G.; Lei, W.; Luo, D.; Deng, Y.; Deng, Z.; Wang, D.; Yu, A.; Chen, Z. Stringed "Tube on Cube" Nanohybrids as Compact Cathode Matrix for High-Loading and Lean-Electrolyte Lithium-Sulfur Batteries. *Energy Environ. Sci.* **2018**, *11*, 2372-2381.

11. Wang, L.; He, Y.-B.; Shen, L.; Lei, D.; Ma, J.; Ye, H.; Shi, K.; Li, B.; Kang, F. Ultra-Small Self-Discharge and Stable Lithium-Sulfur Batteries Achieved by Synergetic Effects of Multicomponent Sandwich-Type Composite Interlayer. *Nano Energy* **2018**, *50*, 367-375.

12. Ghazi, Z. A.; He, X.; Khattak, A. M.; Khan, N. A.; Liang, B.; Iqbal, A.; Wang, J.; Sin, H.; Li, L.; Tang, Z. MoS_2/Celgard Separator as Efficient Polysulfide Barrier for Long-Life Lithium-Sulfur Batteries. *Adv. Mater.* **2017**, *29*, 1606817.

13. Cherian, C. T.; Sundaramurthy, J.; Reddy, M. V.; Suresh Kumar, P.; Mani, K.; Pliszka, D.; Sow, C. H.; Ramakrishna, S.; Chowdari, B. V. Morphologically Robust $NiFe_2O_4$ Nanofibers as High Capacity Li-Ion Battery Anode Material. *ACS Appl. Mater. Interfaces* **2013**, *5*, 9957.

14. Shao, H.; Ai, F.; Wang, W.; Zhang, H.; Wang, A.; Feng, W.; Huang, Y. Crab Shell-

Derived Nitrogen-Doped Micro-/Mesoporous Carbon as an Effective Separator Coating for High Energy Lithium-Sulfur Batteries. *J. Mater. Chem. A* **2017**, *5*, 19892-19900.

15. Wu, H.; Huan, Y.; Wang, D.; Li, M.; Cheng, X.; Bai, Z.; Wu, P.; Peng, W.; Zhang, R.; Ji, Z.; Zou, M.; Yan, X. Hierarchical VS_2 Nano-Flowers as Sulfur Host for Lithium Sulfur Battery Cathodes. *J. Electrochem. Soc.* **2019**, *166*, A188-A194.

16. Cheng, Z.; Xiao, Z.; Pan, H.; Wang, S.; Wang, R. Elastic Sandwich-Type RGO-VS_2/S Composites with High Tap Density: Structural and Chemical Cooperativity Enabling Lithium-Sulfur Batteries with High Energy Density. *Adv. Energy Mater.* **2018**, *8*, 1702337.

17. Xi, K.; He, D.; Harris, C.; Wang, Y.; Lai, C.; Li, H.; Coxon, P. R.; Ding, S.; Wang, C.; Kumar, R. V. Enhanced Sulfur Transformation by Multifunctional FeS_2/FeS/S Composites for High-Volumetric Capacity Cathodes in Lithium-Sulfur Batteries. *Adv. Sci.* **2019**, *6*, 1800815.

18. Wu, J.; Zeng, H.; Li, X.; Xiang, X.; Liao, Y.; Xue, Z.; Ye, Y.; Xie, X. Ultralight Layer-By-Layer Self-Assembled MoS_2-Polymer Modified Separator for Simultaneously Trapping Polysulfides and Suppressing Lithium Dendrites. *Adv. Energy Mater.* **2018**, *8*, 1802430.

19. He, J.; Chen, Y.; Manthiram, A. Vertical Co_9S_8 Hollow Nanowall Arrays Grown on a Celgard Separator as a Multifunctional Polysulfide Barrier for High-Performance Li-S Batteries. *Energy Environ. Sci.* **2018**, *11*, 2560-2568.

20. Dong, Y.; Zheng, S.; Qin, J.; Zhao, X.; Shi, H.; Wang, X.; Chen, J.; Wu, Z. S. All-

Mxene-Based Integrated Electrode Constructed by Ti_3C_2 Nanoribbon Framework Host and Nanosheet Interlayer for High-Energy-Density Li-S Batteries. *ACS Nano* **2018**, *12*, 2381-2388.

21. Sun, J.; Sun, Y.; Pasta, M.; Zhou, G.; Li, Y.; Liu, W.; Xiong, F.; Cui, Y. Entrapment of Polysulfides by a Black-Phosphorus-Modified Separator for Lithium-Sulfur Batteries. *Adv. Mater.* **2016**, *28*, 9797-9803.

22. Guo, Y.; Zhang, Y.; Zhang, Y.; Xiang, M.; Wu, H.; Liu, H.; Dou, S. Interwoven V_2O_5 Nanowire/Graphene Nanoscroll Hybrid Assembled as Efficient Polysulfide-Trapping-Conversion Interlayer for Long-Life Lithium-Sulfur Batteries. *J. Mater. Chem. A* **2018**, *6*, 19358-19370.

23. Zhao, Q.; Zheng, J.; Archer, L. Interphases in Lithium-Sulfur Batteries: Toward Deployable Devices with Competitive Energy Density and Stability. *ACS Energy Lett.* **2018**, *3*, 2104-2113.

24. Peng, H.-J.; Huang, J.-Q.; Cheng, X.-B.; Zhang, Q. Review on High-Loading and High-Energy Lithium-Sulfur Batteries. *Adv. Energy Mater.* **2017**, *7*, 1700260.